Journal Pre-proofs

Experimental evaluation of effective stress intensity factor using thermoelastic stress analysis and digital image correlation

F.A. Díaz, J.M. Vasco-Olmo, E. López-Alba, L. Felipe-Sesé, A.J. Molina-Viedma, D. Nowell

PII: S0142-1123(20)30098-0
DOI: https://doi.org/10.1016/j.ijfatigue.2020.105567
Reference: JIJF 105567

To appear in: *International Journal of Fatigue*

Received Date: 8 November 2019
Revised Date: 19 February 2020
Accepted Date: 24 February 2020

Please cite this article as: Díaz, F.A., Vasco-Olmo, J.M., López-Alba, E., Felipe-Sesé, L., Molina-Viedma, A.J., Nowell, D., Experimental evaluation of effective stress intensity factor using thermoelastic stress analysis and digital image correlation, *International Journal of Fatigue* (2020), doi: https://doi.org/10.1016/j.ijfatigue.2020.105567

Experimental evaluation of effective stress intensity factor using thermoelastic stress analysis and digital image correlation

F.A. Díaz[1], J.M. Vasco-Olmo[1*], E. López-Alba[1], L. Felipe-Sesé[1], A.J. Molina-Viedma[1], D. Nowell[2]

[1] Departamento de Ingeniería Mecánica y Minera, University of Jaén, Jaén, Spain.

[2] Department of Mechanical Engineering, Imperial College London, London, UK.

*corresponding author: jvasco@ujaen.es

Abstract. During the last decades, the debate over the mechanisms governing fatigue crack shielding has been mainly focused on demonstrating the existence of fatigue crack closure and the difficulties on quantifying the induced stress during crack propagation. Hence, most adopted experimental methods have been based on the direct or indirect measurement of contact loads between crack surfaces as the crack starts closing. Nevertheless, these methods depend on many factors sometime difficult to control, which has contributed to question their reliability by many authors. For this reason, two modern well established, full-field, non-contact experimental techniques, namely Thermoelastic Stress Analysis (TSA) and 2D Digital Image Correlation (2D-DIC), have been analysed to evaluate the influence of crack shielding during fatigue experiments conducted on two aluminium alloys (Al2024-T3 and Al7050) tested at different stress ratios. In the particular case of TSA, the technique appears to have a great potential in the evaluation of fatigue crack shielding since crack tip events are inferred directly from the temperature changes occurring at the crack tip rather than from remote data. Experimental data from both techniques have been employed in combination with two different mathematical models based on Muskhelishvili's complex potentials to infer the effective range of stress intensity factor. Results from both techniques agree quite well, showing a variation in the stress intensity factor range as the *R*-ratio changes from 0.1 to 0.5 and illustrating the potential ability of both techniques to account for the shielding effect due to crack closure.

Keywords. Stress intensity factor, Thermoelastic Stress Analysis (TSA), Digital Image Correlation (DIC), crack shielding; fatigue crack growth.

Nomenclature:

A', *B'*, *C'*, *E'*, *F'*:	coefficients on the CJP model for describing crack tip displacement fields
A_N, B_N, a_m, b_n:	complex variables in Muskhelishvili's model to describe different stress states fields
a:	crack length
C_p:	heat capacity at constant pressure
DIC:	Digital Image Correlation
E:	Young's modulus
G:	shear modulus
i:	square root of -1
K:	thermoelastic constant
K_F:	opening mode stress intensity factor in the CJP model
K_I:	mode I stress intensity factor
K_R:	retardation stress intensity factor
K_S:	shear stress intensity factor
R:	ratio between the minimum and the maximum applied load
TSA:	Thermoelastic Stress Analysis
T:	absolute temperature
T_x, T_y:	components of the T-stress in x and y-directions, respectively
U:	notation for stress function
u, *v*:	components of the displacement vector
z:	complex coordinate of the collected points around the crack tip
α:	coefficient of thermal expansion
ρ:	density
κ:	function of Poisson's ratio
ν:	Poisson's ratio
σ_{ys}:	Yield stress
$\Psi(z)$, $\Phi(z)$:	complex stress functions

ς:	complex coordinate in mapping plane
χ:	auxiliary function in Muskhelishvili's model
ρ:	auxiliary function in Muskhelishvili's model

1. Introduction

Fatigue cracks have been one of the main sources of structural failures in real in-service structures. The application of fracture mechanics to engineering design has provided the possibility of understanding further into the study of failure and crack growth mechanisms. But there are still some aspects that remain not fully understood, such a case is the crack closure effect. This lack of understanding arises principally from the difficulties associated in quantifying the phenomenon and measuring its effect on the crack driving force [1].

In the study of crack propagation, the experimental analysis of stresses or displacements around the tip of a growing fatigue crack plays a significant role. Modern experimental techniques, such as digital image correlation (DIC) [2] or thermoelastic stress analysis (TSA) [3], have actively contributed to a better understanding of the different fatigue and failure mechanisms. In this respect, TSA seems to be an extraordinarily suitable technique for studying crack shielding. The technique is non-contacting and provides full-field stress maps from the surface of structural components by measuring small temperature changes at the surface of the structure arising from cyclic loading. Additionally, the potential of TSA for fracture mechanics applications has been recently enhanced with the development of new infrared array detectors. On the other hand, DIC is globally accepted as a powerful technique for analysing fatigue and fracture problems and seems to be very suitable for the evaluation of crack shielding since crack tip displacement fields can be quantified with high level of accuracy [4].

It is well known that crack tip fields can be characterised by stress intensity factors (SIFs) [5]. Different mathematical models for the calculation of SIFs from the analysis of displacement fields have been developed. Some works were based on Williams' expansion series [6] and others on Muskhelisvili's complex potentials [7]. All these methodologies were based on the Multi-Point Over-Deterministic Method (MPODM) developed by Sanford and Dally for calculating SIFs [8]. In recent years, special interest has been focused on the development of the CJP model [9] for characterising crack tip fields since considers the crack shielding effect on the elastic stress field induced by plasticity generated during fatigue crack propagation. This model has been specifically developed as an endeavour to obtain an elastic stress field model that explicitly captures the influences of an embedded region of plasticity surrounding a growing fatigue crack. This plastic enclave is therefore considered to shield the crack from the full influence of the elastic stress field that drives fatigue crack growth. The model further proposes that these plasticity-induced effects can be assessed through incorporation of the influence of interfacial stresses at the elastic-plastic boundary on the elastic stress field ahead of the crack tip. Different works reported by some of the authors of the present work have demonstrated the great potential of the combination between the CJP model and DIC technique to study the shielding effect during fatigue crack growth at constant [10] and variable loading [11]. For this reason, in this work data obtained by DIC technique are compared with those obtained by TSA since enables to infer crack tip events directly from the temperature changes occurring at the tip rather than from remote data. Recently, Nowell and co-workers have shown very interested in the development of the CJP model through two works [12], [13] where some data obtained by the research group of fracture from Jaén were compared with some obtained by them.

Closure mechanisms reduce the effective crack driving force, and hence, the material shows an enhanced resistance to crack growth. Nevertheless, TSA due to its physical nature appears to offer a direct means of measuring the effective crack driving force. This presumed ability arises from the fact that with TSA the near crack tip stress distribution is obtained from the temperature variations on the specimen's surface as a result of the thermoelastic effect, providing a direct assessment of cyclic strain around the crack tip. Hence, the observed crack tip stress pattern is the result of the specimen's response to the applied loading cycle.

However, besides of the presumed potential of TSA to account for shielding mechanisms, most of the work conducted in TSA in relation with fracture mechanics applications has been mainly related to different methods and approaches for the calculation of the range of stress intensity factor from the analysis of thermoelastic images [14]–[18].

In the present paper, TSA and DIC techniques are employed in combination with two mathematical models based on Muskhelishvili's complex potentials to evaluate the influence of shielding during fatigue experiments conducted with two commercial aluminium materials (Al2024-T3 and Al7050-T6) at different R-ratios. The inferred ΔK results illustrate the potential of both techniques for the evaluation of crack shielding during fatigue crack growth.

2. Fundamentals of the optical techniques

In the present work the optical techniques of thermoelastic stress analysis (TSA) and digital image correlation (DIC) are employed to calculate the range of stress intensity factor. Thus, in this section the fundamentals of both techniques are briefly described.

2.1. Fundamentals of TSA

Thermoelastic stress analysis can be defined as a non-contact, non-destructive and non-invasive experimental technique that provides full-field stress maps by measuring temperature changes induced by the thermoelastic effect at the surface of a mechanical component as a result of a periodic change in the applied load. The deformation of a body is always associated with a change in its heat content and consequently, with a change in its temperature. The classical theory of thermoelasticity states that the application of a repetitive loading in a solid produces in it out-of-phase temperature changes that can be related to the variation in the sum of the principal stresses according to the following expression [3]:

$$\Delta T = -\frac{\alpha T}{\rho C_p}\Delta(\sigma_1 + \sigma_2) = K\,T\,\Delta(\sigma_1 + \sigma_2) \qquad (1)$$

Where K is the thermoelastic constant, that depends on the material properties, such as the coefficient of thermal expansion α, the density ρ, and the heat capacity at constant pressure C_p.

The thermoelastic information is normally presented as a vector, where the modulus denotes the magnitude of the thermoelatic signal (Figure 1a), which is proportional to the variation in temperature experienced by the specimen as a result of the thermoelastic effect, and the phase (Figure 1b) denotes the angular shift between the thermoelastic and the loading signal. Under elastic conditions, the phase shift between the thermoelastic response of the material and the loading signal remains constant. However, just ahead of the crack tip the presence of local plasticity leads to a change in the phase shift (Figure 1b). This change in phase is employed to identify the plastic zone and hence to locate the crack tip.

2.2. Fundamentals of DIC

DIC is a full-field optical technique used for displacement measurements in structural or mechanical components. It works analysing a sequence of images of the analysed component from an initial state (undeformed) to a final state (deformed). This technique can be implemented both in 2D (in-plane) and 3D (in and out-of-plane). In this work 2D DIC is implemented since the displacement fields are obtained on a plane specimen. Its implementation comprises the following steps [19]: 1) specimen and experimental equipment preparations, 2) acquisition of a sequence of images and 3) processing of the acquired images.

The specimen surface must have a random grey intensity distribution (a random speckle pattern), which deforms together with the specimen. The speckle pattern can be the natural texture of the specimen surface or artificially made by spraying a random black speckle over a white background applied on the specimen surface. The camera must be placed with its optical axis perpendicular to the specimen surface in order to avoid inaccurate two-dimensional measurements. After preparing the specimen and assembling the set-up, a sequence of images is acquired from an initial or reference state (undeformed state) until a final state (deformed state).

Once the sequence of images has been acquired, its processing is performed. The basic principle of 2D DIC consists on tracking the displacement of points in two recorded images before and after deformation. To compute the displacements at a certain point *P*, a square reference subset centred at point *P* from the reference image is chosen and used to track its corresponding location in the deformed image. To implement 2D DIC, it is necessary to define the region of interest (ROI) in the reference image. This ROI is divided into evenly spaced squares called facets. The displacements are computed at the centre of each facet to obtain full-field deformation.

To evaluate the degree of similarity between the reference and the deformed facet, a correlation criterion must be defined. The most commonly employed correlation criteria are cross-correlation (CC) and sum-squared difference correlation (SSD). Further information about these correlation criteria can be found in reference [2].

3. Description of the models characterising crack tip fields

The purpose of the current work is to assess the effective stress intensity factor range on growing fatigue cracks. Several models for characterising crack tip fields can be found in the literature. Among them, that based on Muskhelishvili's complex potential and the CJP model have been adopted since it has been reported that they provide the most accurate determination of stress intensity factor by using TSA [20], [21] and DIC [10], [11], respectively. For this reason these two models are used in this work to calculate stress intensity factor.

3.1. Model based on Muskhelishvili's complex potentials

According to the theory of plane elasticity, stresses occurring in a body can be expressed as a single function called a stress function. If the equilibrium conditions are satisfied and in absence of body forces, it can be written as:

$$\begin{gathered}\frac{\partial \sigma_x}{\partial x}+\frac{\partial \tau_{xy}}{\partial y}=0\\ \frac{\partial \sigma_y}{\partial y}+\frac{\partial \tau_{xy}}{\partial x}=0\end{gathered} \tag{2}$$

In addition, according to the theory of plane elasticity there always exists a function *U(x,y)* (Airy function) that satisfies the following equation:

$$\sigma_x + \sigma_y = U \tag{3}$$

Muskhelishvili [22] showed that every biharmonic function *U(x,y)* may be represented by two functions φ and χ of the complex variable $z=x+iy$. Therefore, the stress function takes the form:

$$U = \Re\left\{\bar{z}\varphi(z) + \chi(z)\right\} \tag{4}$$

Where the bar denotes the conjugate and $\Re$, refers to the real part in complex notation.

Substituting equation 4 in equation 3 it can be obtained:

$$\sigma_x + \sigma_y = 2\left[\varphi'(z) + \overline{\varphi'(z)}\right] = 2\left[\Phi(z) + \overline{\Phi(z)}\right] = 4\Re\Phi(z) \tag{5}$$

with $\Phi(z) = \varphi'(z)$ and the prime to denote the derivative.

Nurse and Patterson [23] introduced some modifications to the original approach developed by Muskhelishvili. It was assumed that the state of stress at the crack tip in the cracked body under consideration could be represented by the stress at the crack tip in an infinite plate in a generalised state of stress based on Muskhelishvili's complex potentials in the form of Fourier series. In addition, as in Muskhelishvili's model the boundary conditions at the crack surfaces were satisfied by a conformal mapping equation [22]. Based on this premises, the following two complex potentials are defined as:

$$\begin{aligned} \Phi(\varsigma) &= \sum_{N=0}^{\infty} A_N \varsigma^{2N} + \sum_{m=1}^{\infty} \frac{a_m}{\varsigma^{2m}} \\ \Psi(\varsigma) &= \sum_{N=0}^{\infty} B_N \varsigma^{2N} + \sum_{n=1}^{\infty} \frac{b_n}{\varsigma^{2n}} \end{aligned} \tag{6}$$

Where A_N, B_N, a_m and b_n are complex variables and are used to describe different states of stress. ς represents the complex coordinates of points surrounding the crack tip in the mapping plane.

To satisfy the boundary conditions the series of parameters a_m and b_n were solved by equating terms of power of φ. As a result, the following expressions for a_m and b_n were obtained:

$$a_m = A_0 + \overline{A_0} + B_0 + \sum_{j=1}^{m}(4j)\overline{A_j} - (2m+1)\overline{A_m} - \overline{B_m}$$
$$b_n = A_0 + \overline{A_0} + B_0 + \sum_{k=1}^{n}(4k)a_k - (2n+1)a_k - \overline{A_n} \tag{7}$$

Where the over bar denotes the conjugate.

Subsequently, the expression for the complex potentials was calculated by inserting equation 7 into equation 6 and rearranging the terms.

$$\Phi(\varsigma) = A_0 + \frac{A_0 + \overline{A_0} + B_0}{(\varsigma^2 - 1)} + \sum_{N=1}^{\infty}\left[\left(\frac{2N}{\varsigma^{2N}}\right)\left(\frac{\varsigma^2+1}{\varsigma^2-1}\right)\overline{A_N} - \frac{\overline{A_N}}{\varsigma^{2N}} - \frac{\overline{B_N}}{\varsigma^{2N}} + A_N\varsigma^{2N}\right]$$
$$\Psi(\varsigma) = B_0 + \frac{B_0 + \overline{B_0}}{(\varsigma^2-1)} + 2\left(A_0 + \overline{A_0} + \overline{B_0}\right)\frac{\varsigma^2(\varsigma^2-1)}{(\varsigma^2-1)^3} +$$
$$+\sum_{N=1}^{\infty}\left[\left(\frac{4N}{\varsigma^{2N}}\right)\frac{(\varsigma^4-1)(\varsigma^2+1)}{(\varsigma^2-1)^3}\overline{A_N} + \left(\frac{8N}{\varsigma^{2N}}\right)\frac{\varsigma^2(\varsigma^2+1)}{(\varsigma^2-1)^3}\overline{A_N}\right] - \tag{8}$$
$$-\sum_{N=1}^{\infty}\left[\left(\frac{4N}{\varsigma^{2N}}\right)\left(\frac{\varsigma^2+1}{\varsigma^2-1}\right)\overline{A_N} - \left(\frac{2N}{\varsigma^{2N}}\right)\left(\frac{\varsigma^2+1}{\varsigma^2-1}\right)\overline{B_N} + \frac{\overline{B_N}}{\varsigma^{2N}} - B_N\varsigma^{2N}\right]$$

Finally substituting the first part of equation 8 into equation 5, an expression for the first stress invariant can be derived:

$$\sigma_x + \sigma_y = 2\left[\Phi(\varsigma) + \overline{\Phi(\varsigma)}\right] =$$
$$= 4\Re\left[A_0 + \frac{A_0 + \overline{A_0} + B_0}{(\varsigma^2-1)} + \sum_{N=1}^{\infty}\left[\left(\frac{2N}{\varsigma^{2N}}\right)\left(\frac{\varsigma^2+1}{\varsigma^2-1}\right)\overline{A_N} - \frac{\overline{A_N}}{\varsigma^{2N}} - \frac{\overline{B_N}}{\varsigma^{2N}} + A_N\varsigma^{2N}\right]\right] \tag{9}$$

Expression 9 provides the first stress invariant as a function of Fourier series coefficients and the polar coordinates in the mapping plane. The Fourier series coefficients depend on the problem and they are unknowns, that can be obtained by fitting the mathematical model to experimental data corresponding to the sum of principal stresses provided by TSA.

3.2. CJP model

The CJP model is a mathematical model developed by Christopher, James and Patterson [9] based on Muskhelishvili's complex potentials [22]. The authors postulated that the plastic enclave which exists around the tip of a fatigue crack and along its flanks will shield the crack from the full influence of the applied elastic stress field and that crack tip shielding includes the effect of crack flank contact forces (so-called crack closure) as well as a compatibility-induced interfacial shear stress at the elastic-plastic boundary. James et al. [9] provided a schematic idealisation of forces that is repeated here as

Figure 2, which illustrates the forces believed to be acting at the interface between the plastic zone and the surrounding elastic material. These forces include [9]: F_{Ax} and F_{Ay} are the reaction forces to the remote load that generates the crack tip stress fields traditionally characterised by the stress intensity factor K_I; F_T is the force due to the T-stress; F_{Px} and F_{Py} are the forces induced by the compatibility requirements on the elastic-plastic boundary near the crack tip, resulting from the permanent deformation in the plastic zone around the crack tip, which is extensive in the direction perpendicular to the crack and contractive along the crack due to the effect of the Poisson's ratio; F_S is the force induced by the compatibility requirements on the elastic-plastic boundary of the crack wake; F_C is the contact force arising from the plastic wake contact effect transmitted to the elastic-plastic boundary of the crack wake. In the original formulation of this model, crack tip displacement fields [9] were characterised as:

$$\begin{aligned}2G(u+iv)=\kappa&\left[-2(B'+2E')z^{1/2}+4E'z^{1/2}-2E'z^{1/2}ln(z)-\frac{C'-F'}{4}z\right]\\&-z\left[-(B'+2E')\bar{z}^{-1/2}-E'\bar{z}^{-1/2}\overline{ln(z)}-\frac{C'-F'}{4}\right]\\&-\left[A'\bar{z}^{1/2}+D'\bar{z}^{1/2}\overline{ln(z)}-2D'\bar{z}^{1/2}+\frac{C'+F'}{2}\bar{z}\right]\end{aligned}\qquad(10)$$

Where $G=\dfrac{E}{2(1+\nu)}$ is the shear modulus, E and v are the Young's modulus and Poisson's ratio of the material, respectively; and $\kappa=\dfrac{3-\nu}{1+\nu}$ for plane stress or $\kappa=3-4\nu$ for plane strain. In the mathematical analysis, the assumption $D' + E' = 0$ must be made in order to give an appropriate asymptotic behaviour of the stress along the crack flank [9]. Therefore, crack tip displacement fields are defined from five coefficients: A', B', C', E' and F'.

The CJP model provides three stress intensity factors to characterise the stress and displacement fields around the crack tip; an opening mode stress intensity factor K_F, a retardation stress intensity factor K_R, a shear stress intensity factor K_S and also gives the T-stress.

The opening mode stress intensity factor K_F is defined using the applied remote load traditionally characterised by K_I but that is modified by force components derived from the stresses acting across the elastic-plastic boundary and which therefore influence the driving force for crack growth. Thus, unlike the classical K_I, K_F includes the effect of plasticity-induced crack shielding and it is linear with the load as long as there is no shielding effect. K_F is defined from the asymptotic limit of σ_y as $x \to +0$, along $y = 0$, i.e. towards the crack tip on the crack plane ahead of the crack tip:

$$K_F = \lim_{r \to 0}\left[\sqrt{2\pi r}\left(\sigma_y + 2E' r^{-1/2} \ln r\right)\right] = \sqrt{\frac{\pi}{2}}\left(A' - 3B' - 8E'\right) \tag{11}$$

The retardation stress intensity factor K_R characterises forces applied in the plane of the crack and which provide a retarding effect on fatigue crack growth. Thus, K_R is evaluated from σ_x in the limit as $x \to -0$, along $y = 0$, i.e. towards the crack tip along the crack flank:

$$K_R = \lim_{r \to 0}\left[\sqrt{2\pi r}\,\sigma_x\right] = -(2\pi)^{3/2} E' \tag{12}$$

The shear stress intensity factor K_S characterises compatibility-induced shear stress along the plane of the crack at the interface between the plastic enclave and the surrounding elastic field and is derived from the asymptotic limit of σ_{xy} as $x \to -0$, along $y = 0$, i.e. towards the crack tip along the crack wake:

$$K_S = \lim_{r \to 0}\left[\sqrt{2\pi r}\,\sigma_{xy}\right] = \mp\sqrt{\frac{\pi}{2}}\left(A' + B'\right) \tag{13}$$

A positive sign indicates $y > 0$, and a negative sign that $y < 0$.

The T-stress, which is found as components T_x in the x-direction and T_y in the y-direction is given by:

$$\begin{aligned} T_x &= -C' \\ T_y &= -F' \end{aligned} \tag{14}$$

4. Experimental details

Table 1 presents mechanical property data for AA2024-T3 and AA7050-T6 obtained from tension tests. All CT specimens had a thickness of 1 mm and dimensions in accordance with ASTM E647 [24] as shown in Figure 3, and were subject to constant amplitude loading with a maximum load of 600 N. Tests were performed at stress ratio values of 0.1, 0.3 and 0.5.

The two surfaces of each specimen were treated using different methods to enable simultaneous measurements of displacements by DIC and stresses by TSA. The surface used for the DIC study was sprayed with a random black speckle pattern over a white background (shown in Figure 4a), while the other surface of the specimen (used for the TSA implementation) was sprayed with a black matt paint in order to increase the surface emissivity. The experimental set-up for fatigue testing and the equipment for data acquisition are shown in Figure 4b. Fatigue tests were conducted on a 25 kN servohydraulic machine (MTS 370.02) at a cycling frequency of 10 Hz.

DIC images were captured with a CCD camera (AVT Stingray F-504 B/C) placed perpendicularly to the specimen surface, focusing with a macro-zoom lens (MLH-10X EO) to increase the spatial resolution around the crack tip. The camera and the lens were set up to give a resolution of 8.8 μm/pixel (field of view of 14.1 x 10.6 mm), with the crack path in the centre of the image (as seen in Figure 4a). The speckled surface of the specimen was illuminated with a fibre optic light source (Fiber-Lite DC-950) to enable a better observation of the speckle pattern and improved image processing. Image processing was performed by Vic-2D [25] from Correlated Solutions Company using 25 pixels as subset size and a step value of 1 pixel to obtain the maximum resolution for the displacement maps. Figure 5 shows an example of horizontal and vertical displacement maps for a crack length of 9.13 mm and a load level of 600 N.

The equipment employed for TSA analysis consisted of a cooled infrared camera FLIR X6581SC. This system incorporates a focal plane array In-Sb sensor that makes it possible to simultaneously collect thermoelastic data from a 640 x 512 pixels window at an adjustable frame rate up to 303 frames per second (figure 4b). The infrared system has a thermal resolution below than 25 mK which for the experiments conducted implied a stress sensitivity lower than 8 MPa. For TSA measurements a 50 mm lens with a 10 mm extension ring was employed providing a spatial resolution of 41 μm/pixel (field of view of 26.2 x 21 mm). Thermal images were processed using IRTA software (produced by DES SLR) to obtain the variation in the sum of principal stress.

Thermoelastic images were calibrated using the same samples employed for fatigue testing. Several times during the experiment, the calibration constant *A* was recalculated to check that no changes on its value were occurring. For this purpose, the variation of the sum of principal stresses was calculated from DIC measurements at the applied load range. Simultaneously, a TSA image (uncalibrated) was captured for the same load range. To calculate the thermoelastic constant *A* a set of data points at a certain distance from the crack tip were collected from both images at the same exact location (from DIC units were MPa and for TSA units were Thermal Units). Finally, a least squares fitting of both set of data was performed to obtain the thermoelastic constant. The value for *A* did not change over the tests and was 8.77 MPa/Thermal Unit for the Al-2024-T3 and 8.82 MPa/Thermal Unit for the Al-7050, respectively

For a direct comparison between the obtained results with both techniques, it was essential to analyse the same crack length by both techniques. According to this, as all specimens had a thickness of 1 mm, the crack length measured on each side was practically the same, which did not have a negative impact on the comparison between techniques.

5. Experimental methodology for determining the stress intensity factor

In this section the adopted experimental methodology for calculating the SIFs from stress and displacement analysis by TSA and DIC, respectively, is described. The multi-point over-deterministic method developed by Sanford and Dally [8] forms the basis of this process. The models are valid only for the elastic field near the crack tip singularity and hence it was necessary to identify the near-tip zone where valid experimental data could be obtained. An annular mesh (Figure 6) was therefore defined with an inner radius large enough to avoid including plastic deformation at the crack tip and an outer radius that lies within the region dominated by the elastic stress singularity.

For DIC, the inner radius is identified by estimating the plastic deformation extension at the crack tip from the implementation of Von Mises yield criterion [26] to establish the region around the crack tip where the stress values are higher than the yield stress of the material (Figure 6a). In addition, the vertical displacement field was used to identify the outer radius by observing changes in the field orientation that originate from the interaction between the singularity dominated region and that dominated by specimen edge effects. This limit is easily identified because the displacement field orientation becomes straight and perpendicular to the crack (observed in Figure 6a).

In the case of TSA, inner radius was obtained by looking at the phase map (Figure 1b) to identify the area near the crack tip where adiabatic conditions were lost as a result of heat generation due to plastic work at the crack tip (region A in Figure 6b). The outer radius was set by identifying the region ahead of the crack tip where a linear behaviour of the inverse square of the maximum thermoelastic signal (horizontal) against the vertical distance from the crack tip was observed, as described by Stanley and Chan [14] (end of region B in Figure 6c). Subsequently, the variation in the sum of principal stresses at the crack dominated zone (Figure 6a) was extracted from thermoelastic images at the locations of the annular mesh, and these values were combined with a mathematical model describing the variation in the sum of principal stress ahead of the crack. The adopted model for TSA data was based on Muskhelishvili's complex potentials and it was implemented adopting the MPOD method [8]. As a result, the stress intensity factor range was inferred from different thermoelastic images corresponding at different crack lengths and *R*-ratios. From the inferred ΔK values an estimation of K_{open} was calculated as $K_{open} = K_{max} - \Delta K_{TSA}$. Where K_{max} is obtained from equation 15 considering P_{max} instead of ΔP.

6. Results and discussion

As mentioned above TSA and DIC are compared by calculating the range of stress intensity factor. In the case of TSA, this value is directly obtained from the material response due to a temperature variation during applying the fatigue cycle. However, the stress intensity factor range by DIC is obtained as the difference between the maximum and minimum values of K_F obtained for the different measured crack lengths ($\Delta K_{DIC} = K_{F,max} - K_{F,min}$). Figure 7 shows an example with the variation of K_F values along a full loading cycle at low and high stress ratio values. K_F vs P plot for 2024-T3 specimen tested at R=0.1 corresponding to a crack length of 4.63 mm is presented in Figure 7a, whilst a similar plot is shown in Figure 7b for 7050-T6 specimen tested at R=0.5 for a crack length of 8.63 mm. In addition, the nominal values of stress intensity factor (equation 15) according to ASTM E 647 [24] are also plotted to establish a comparison between the experimental and nominal trends.

$$\Delta K_{nominal} = \frac{\Delta P}{B\sqrt{W}} \frac{2+\frac{a}{W}}{\left(1-\frac{a}{W}\right)^{3/2}} \left[0.886 + 4.64\frac{a}{W} - 13.32\left(\frac{a}{W}\right)^2 + 14.72\left(\frac{a}{W}\right)^3 - 5.6\left(\frac{a}{W}\right)^4\right] \quad (15)$$

Where $\Delta K_{nominal}$ is the range of stress intensity factor, ΔP is the loading range, a is the crack length, and B and W are the thickness and the width of the specimen, respectively.

In the case of the specimen tested at high stress ratio (Figure 7b), the K_F values closely follow the trend in the nominal K_I values. In contrast, in the case of the specimen tested at low R-ratio, K_F deviates above the nominal K_I once the values fall below approximately 7 MPa·m$^{1/2}$, which corresponds to a load level of 200 N. This behaviour is similar to that reported by Elber [27], [28] when he originally defined plasticity-induced crack closure. He noticed an anomaly in the elastic compliance of fatigue specimens, where at high loads, the measured compliance agreed with that obtained from standard expressions for fracture mechanics, whilst at low load; the compliance was close to that for an uncracked specimen. Elber attributed this variation in compliance to contact between crack surfaces (i.e. crack closure) in the lower part of the load cycle as a consequence of the residual tensile plastic deformation left in the wake of a fatigue crack tip.

In Figure 8 it is plotted a comparison of $K_{nominal}$, $K_{F.max}$ maximum and $K_{F,min}$ obtained from DIC (employing the CJP model) and an estimation of K_{open} obtained from TSA results. For the case of experiments conducted at low R-ratio, $K_{F,min}$ and K_{open} show higher values than $K_{nominal}$ at the minimum applied load. This illustrates the ability of CJP and Muskhelishvili's models to infer the shielding effect due to the premature closure of the crack. This effect was not observed when the analysis was performed at a higher R-ratio, where similar $K_{F,min}$ and K_{open} values were obtained at minimum load. It is important to notice that the CJP model, due to its mathematical formulation cannot be employed with TSA data. However, due to the physical nature of TSA, the amplitude of the thermoelastic signal is directly related with the crack driving force for the fatigue advance [21]. For this reason, a purely elastic model as Muskhelishvili's, is able to account for the shielding effect due to crack closure. This issue is supported by Figure 9 where it has been performed a comparison of ΔK at different R-ratios. For R=0.5 both techniques provide very similar values that agreed with $\Delta K_{nominal}$. On the other hand, for R=0.1 experimental ΔK values obtained by DIC and TSA again provides very similar results but in both cases are lower than $\Delta K_{nominal}$. This demonstrates the ability of both techniques to account for the effective ΔK, that is related with a retardation effect on fatigue crack growth due to the shielding effect arising as a fatigue crack is growing.

7. Conclusions

The influence of crack shielding on fatigue crack growth has been experimentally evaluated in two different aluminium alloys (2024-T3 and 7050-T6) using Thermoelastic Stress Analysis (TSA) and Digital Image Correlation (DIC). Crack shielding effect has been quantified from the calculation of the effective range of stress intensity factor for different fatigue tests conducted at stress ratio values of 0.1 and 0.5. Both techniques have been combined with two different elastic models for characterising crack tip fields, the CJP model in the case of DIC and that model based on Muskhelishvili's complex potentials for TSA. The CJP model has been specifically developed to capture the shielding effects of the plastic enclave from the full influence of the elastic stress field that drives fatigue crack growth. It is to be noticed that the CJP model, due to its mathematical formulation, cannot be employed with TSA. However, due to the physical nature of the technique, the thermal response of the material is directly related with the crack driving force during fatigue crack growth. For this reason, TSA has a great potential in the evaluation of fatigue crack shielding since crack tip events are directly inferred from temperature variation occurring at the tip. Results obtained from both techniques show a great level of agreement, observing a variation in the range of stress intensity factor as the stress ratio changes from 0.1 to 0.5 and highlighting the potential ability of both techniques to account for the shielding effect during fatigue crack growth.

Acknowledgements

The authors gratefully acknowledge the financial support from the Spanish Government through the research project “Proyecto de Investigación de Excelencia del Ministerio de Economía y Competitividad MAT2016-76951-1-P”, without which this work could not have been performed. Professor Nowell is also thanked for helpful discussions during Dr Vasco-Olmo’s research visit to Oxford in 2018 financed by “Ministerio de Educación, Cultura y Deporte” through the grant “Estancias de movilidad en el extranjero ‘José Castillejo’ para jóvenes doctores (convocatoria 2017)”.

References

[1] James, MN. Some unresolved issues with fatigue crack closure – measurement, mechanism and interpretation problems. Ninth International Conference on Fracture 1997; 5: 2403–2414, Pergamon Press, Sydney, Australia.

[2] Sutton MA, Orteu JJ, Schreier HW. Image Correlation for Shape, Motion and Deformation Measurements: Basic Concepts, Theory and Applications. New York: Springer Science + Business Media, 2009.

[3] Thomson W (Lord Kelvin). On the thermoelastic, thermomagnetic, and pyroelectric properties of matters. Phil Mag 1878; 5: 4–27.

[4] Chu TC, Ranson WF, Sutton MA, Peters WH. Applications of digital-image correlation technique to experimental mechanics. Exp Mech 1985; 25: 232–244.

[5] Ewalds HL, Wanhill RJH. Fracture Mechanics. London: Edward Arnold, 1991.

[6] Yates JR, Zanganeh M, Tai YH. Quantifying crack tip displacement fields with DIC. Eng Fract Mech 2010; 77: 2063–2076.

[7] López-Crespo P, Shterenlikht A, Patterson EA, Withers PJ, Yates JR. The stress intensity factors of mixed mode cracks determined by digital image correlation. J Strain Anal Eng Design 2008; 43: 769-80.

[8] Sanford RJ, Dally JW, A general method for determining mixed-mode stress intensity factors from isochromatic fringe patterns. Eng Fract Mech 1979; 11: 621–633.

[9] James MN, Christopher CJ, Lu Y, Patterson EA. Local crack plasticity and its influences on the global elastic stress field. Int J Fatigue 2013; 46: 4-15.

[10] Vasco-Olmo JM, Díaz FA, García-Collado A, Dorado R. Experimental evaluation of crack shielding during fatigue crack growth using digital image correlation. Fatigue Fract Eng Mater Struct. 2015; 38: 223–237.

[11] Vasco-Olmo JM, Díaz FA. Experimental evaluation of the effect of overloads on fatigue crack growth by analysing crack tip displacement fields. Eng Fract Mech 2016; 166: 82–96.

[12] Nowell D, Dragnevski KI, O'Connor SJ. Investigation of fatigue crack models by micro-scale measurement of crack tip deformation. Int J Fatigue 2018; 115: 20–26.

[13] Nowell D, Nowell SC. A comparison of recent models for fatigue crack tip deformation. Theoretical and Applied Fracture Mechanics 2019; 103: 102299.

[14] Stanley P, Chan WK. The determination of stress intensity factors and crack tip velocities from thermoelastic infrared emissions. Proc. of International conference of fatigue of engineering materials and structures, c262, IMechE, Sheffield, UK, 1986: 105–114.

[15] Pukas SR. Theoretical considerations for determining stress intensity factors via thermoelastic stress analysis. Stress analysis by Thermoelastic Technique, Proc. SPIE 1987; 731: 88–101.

[16] Dulieu-Barton JM, Fulton MC, Stanley P. The analysis of thermoelastic isopachic data from crack tip stress fields. Fatigue Fract Eng Mater Struct 2000; 23: 303–313.

[17] Lesniak JR, Bazile DJ, Boyce BR, Zickel MJ, Cramer KE, Welch CS. Stress intensity measurement via infrared focal plane array. Non-traditional Methods of Sensing Stress, Strain, and Damage in Materials and Structures, ASTM STP 1318, Philadelphia 1997.

[18] Tomlinson RA, Nurse AD, Patterson EA. On determining stress intensity factors for mixed mode cracks from thermoelastic data. Fatigue Fract Eng Mater Struct 1997; 20: 217–226.

[19] Pan B, Qian K, Xie H, Asundi A. Two-dimensional digital image correlation for in-plane displacement and strain measurement: a review. Measurement Science and Technology. 2009; 20: 1–17.

[20] Díaz FA, Patterson EA, Tomlinson RA, Yates JR. Measuring stress intensity factors during fatigue crack growth using thermoelasticity. Fatigue Fract Eng Mater Struct. 2004; 27: 571–583.

[21] Díaz FA, Patterson EA, Yates JR. Assessment of effective stress intensity factors uing thermoelastic stress analysis. J Strain Anal Eng Design. 2009; 44: 621–631.

[22] Muskhelishvili NI. Some Basic Problems of the Mathematical Theory of Elasticity. Groningen: Noordhoff International Publishing, 1977.

[23] Nurse AD, Patterson EA. Determination of the predominantly mode II stress intensity factors from isochromatic data. Fatigue Fract Eng Mater Struct 1993; 16(12): 1339–1354.

[24] ASTM, E 647 Standard Test Method for Measurement of Fatigue Crack Growth Rates. 2015, American Society for Testing and Materials: Philadelphia, PA.

[25] https://www.correlatedsolutions.com/vic-2d/

[26] Vasco-Olmo JM, James MN, Christopher CJ, Patterson EA, Díaz FA. Assessment of crack tip plastic zone size and shape and its influence on crack tip shielding. Fatigue Fract Eng Mater Struct. 2016; 39: 969–981.

[27] Elber W. Fatigue crack closure under cyclic tension. Eng Fract Mech 1970; 2: 37–45.

[28] Elber W. The significance of fatigue crack closure. PA: Damage Tolerance in Aircraft Structures, ASTM STP 486, American Society for Testing and Materials; 1971, 230–242.

Table 1. Mechanical properties of the 2024-T3 and 7050-T6 aluminium alloys

Mechanical property	Unit	Aluminium alloy and value	
		2024-T3	7050-T6
Young's modulus, E	GPa	72.3	71.7
Yield stress, σ_{YS}	MPa	348	546
Poisson's ratio, v	-	0.33	0.33

Figures

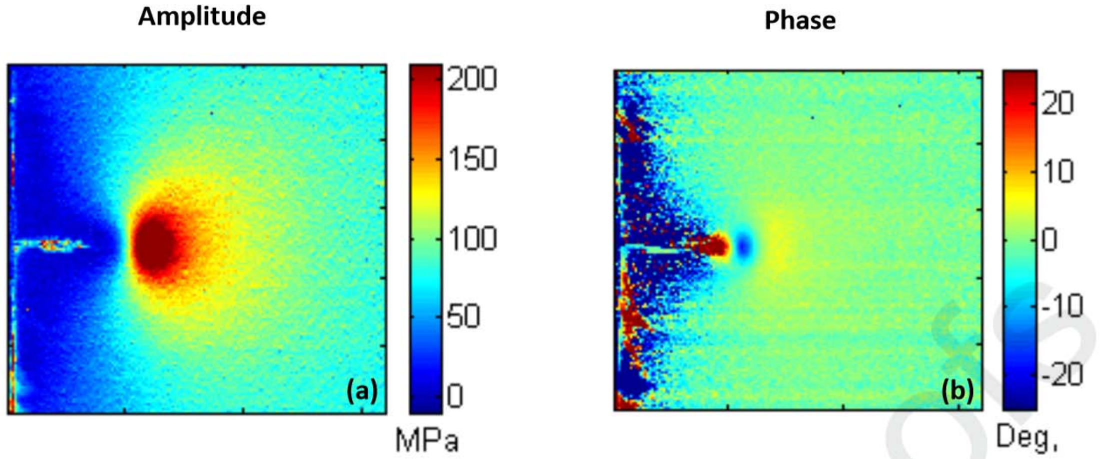

Figure 1 Typical thermoelastic images for a 6.57 mm crack at a load ratio of 0.5 for aluminium 2024-T3. (a) Amplitude of the thermoelastic signal. (b) Phase shift between the material thermoelastic response and the loading signal.

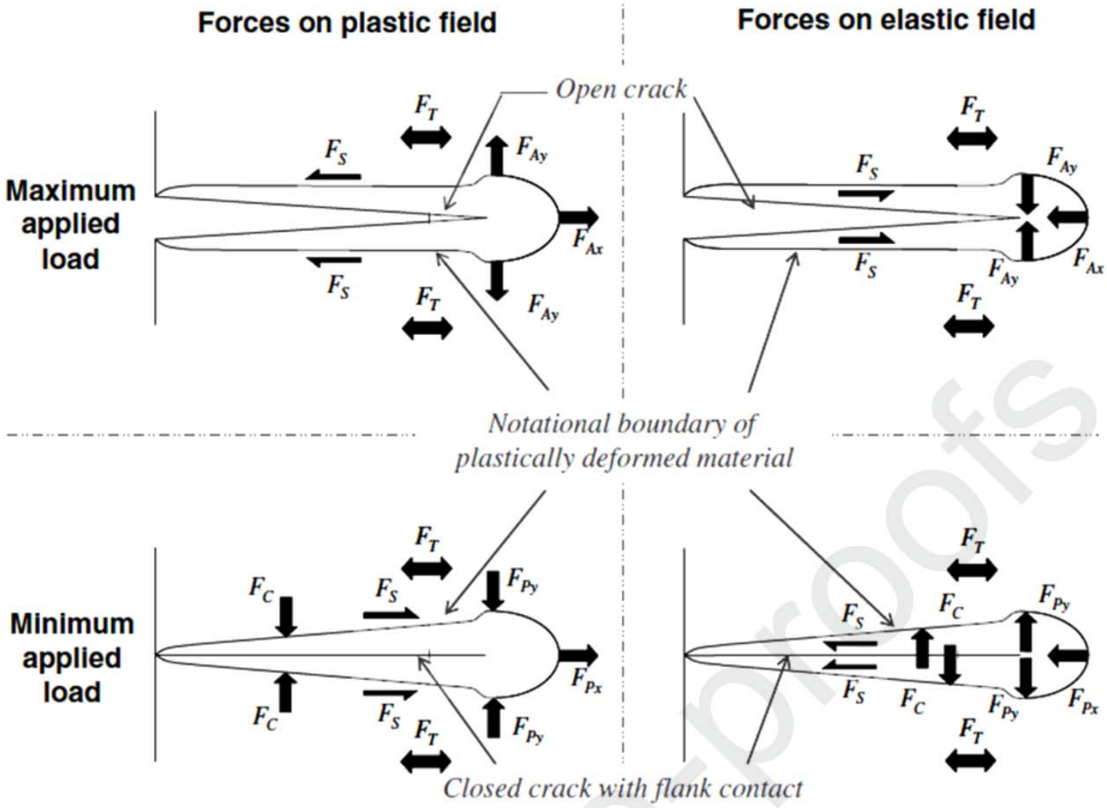

Figure 2 Schematic diagram illustrating the forces acting at the interface of the plastic zone and the surrounding elastic material [9].

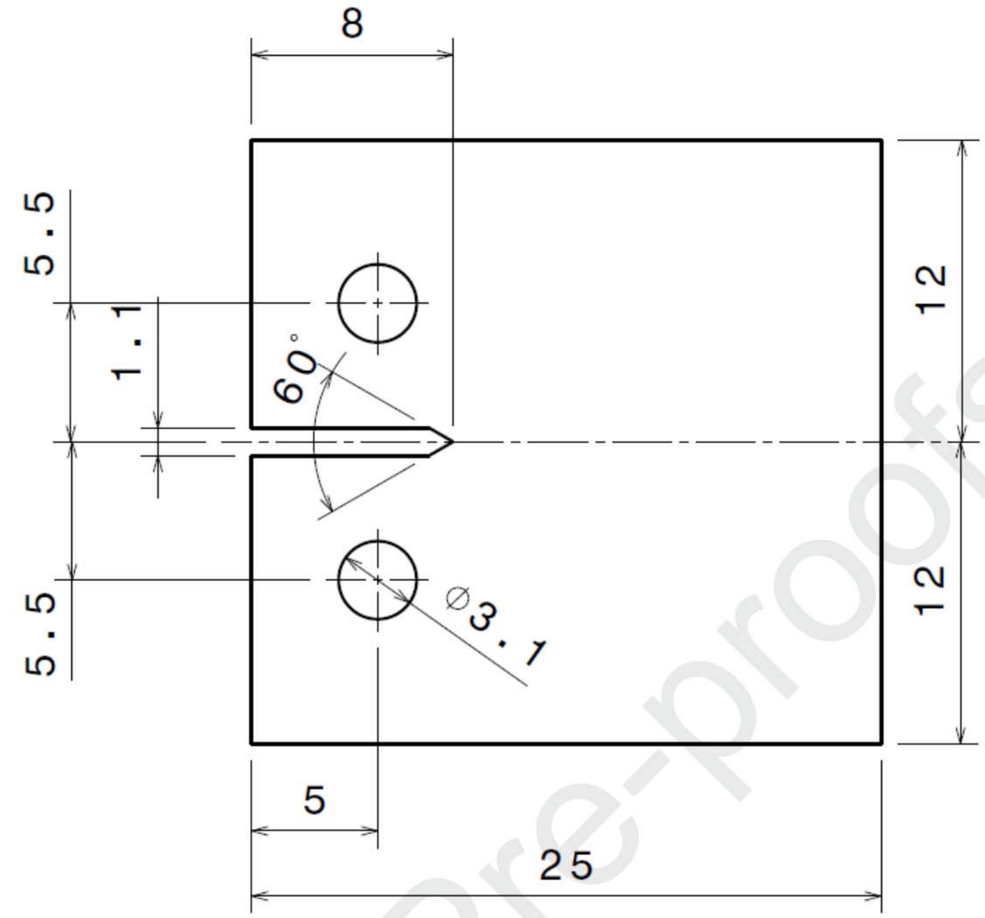

Figure 3 Dimensions (mm) of the CT specimens [24] tested in the lab.

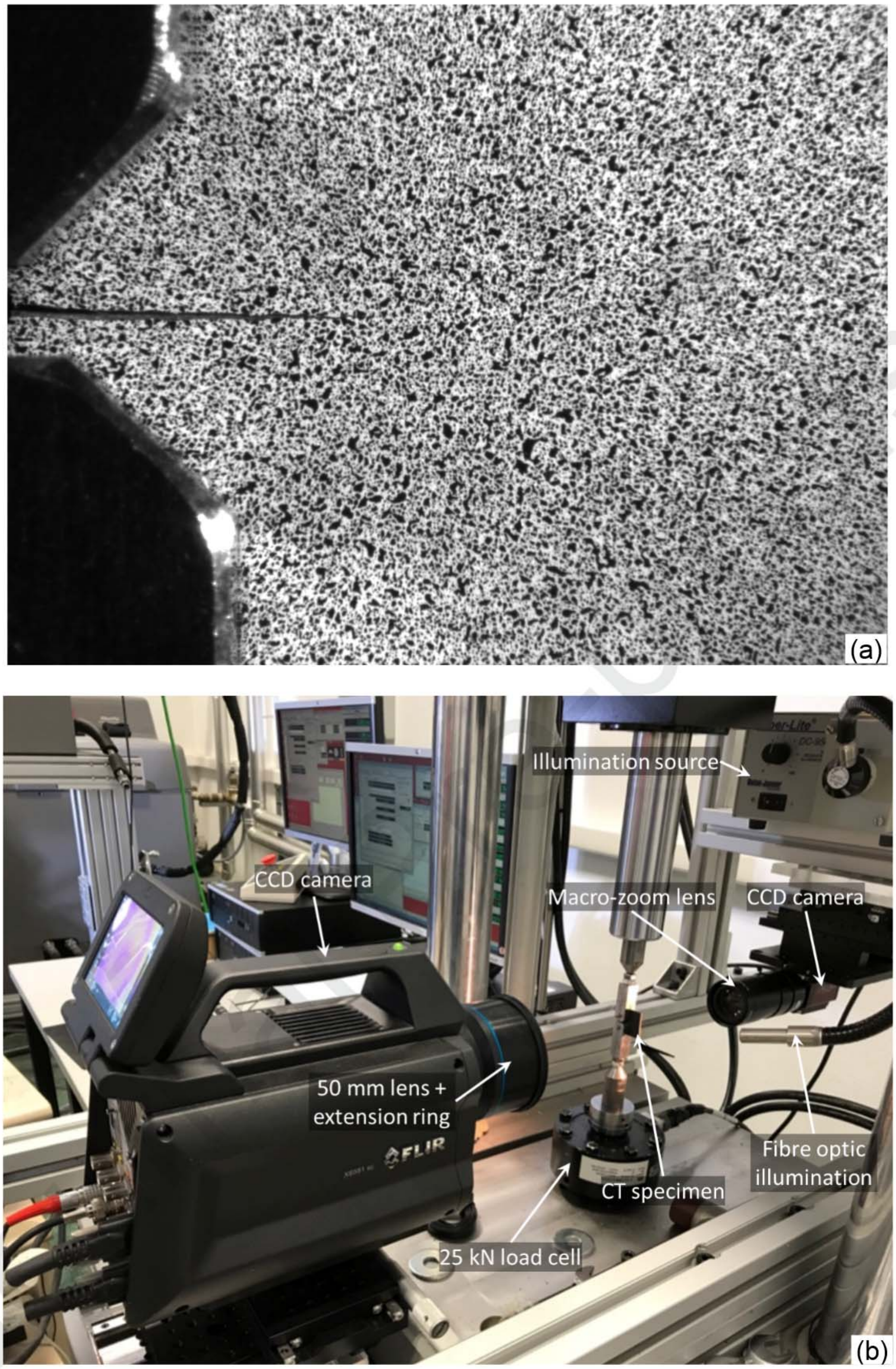

Figure 4 (a) Image showing the speckle pattern applied onto the specimen surface for implementing DIC. (b) Experimental set-up for fatigue testing and data acquisition.

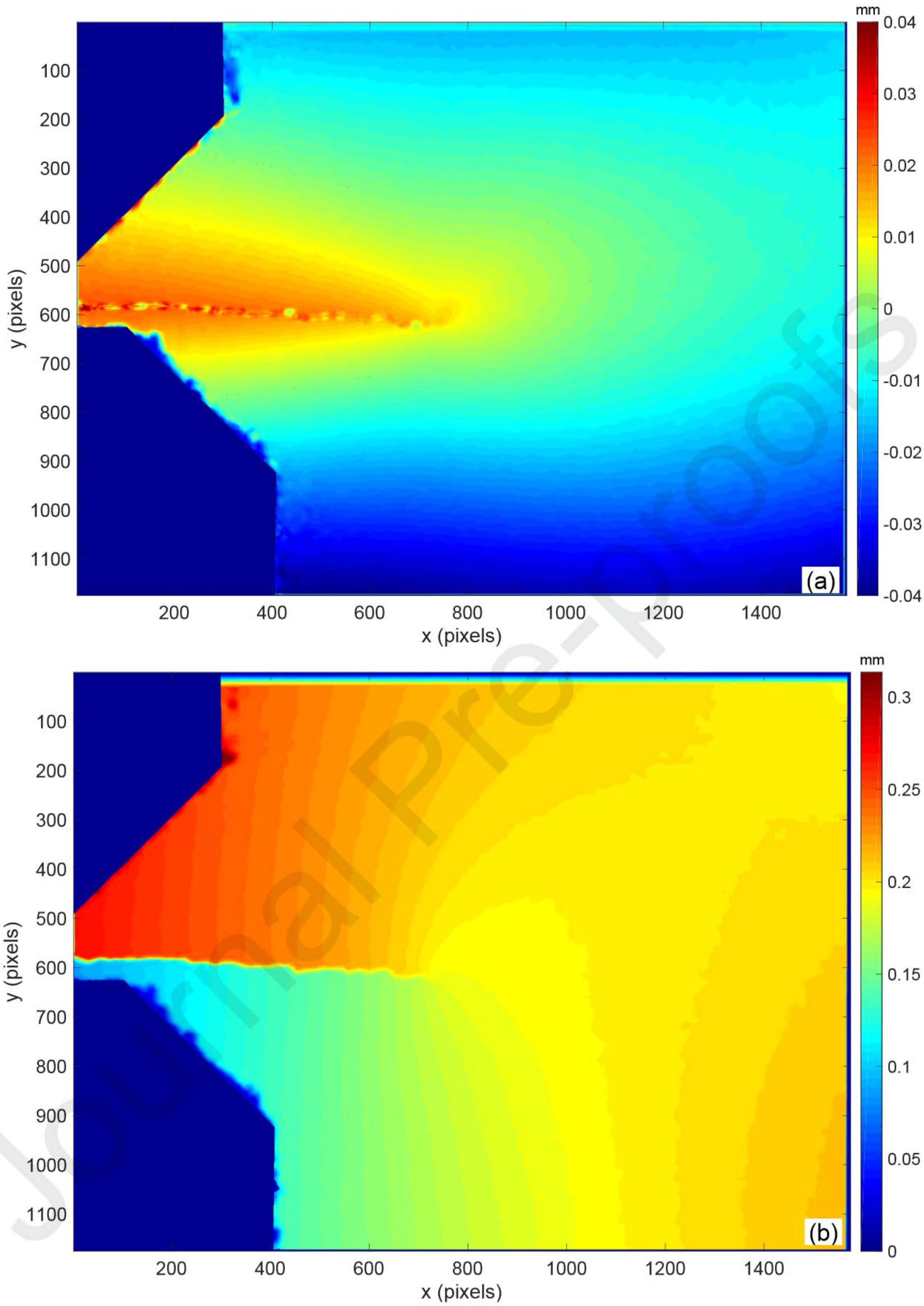

Figure 5 (a) Horizontal and (b) vertical displacement maps obtained by 2D-DIC for a crack length of 9.13 mm at a load level of 600 N.

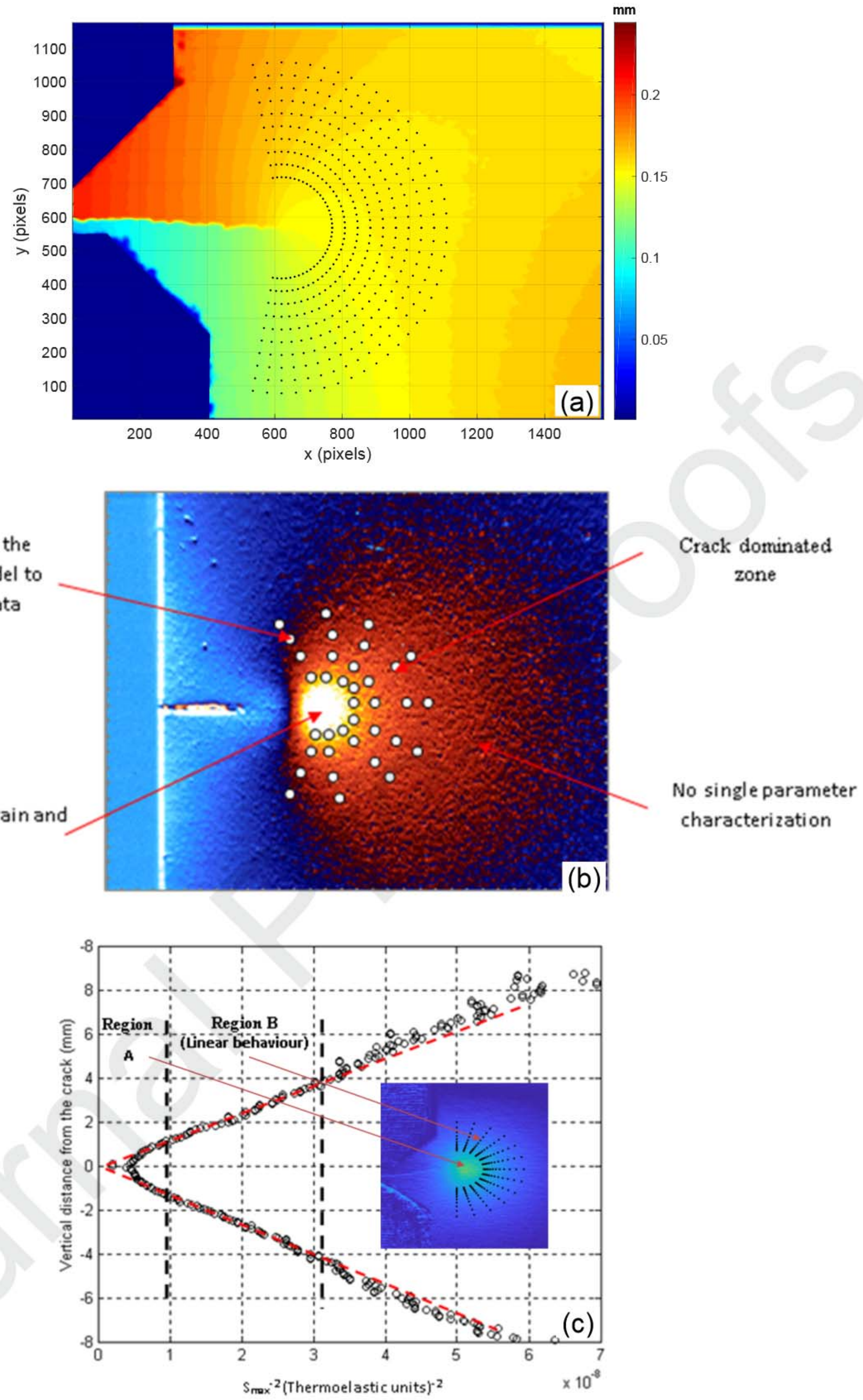

Figure 6 Annular mesh of data points used to define the appropriate near-tip region for the calculation of the SIFs by DIC (a) and TSA (b). c) Graph of showing the linear relationship between the vertical distance from the crack tip and $(\sigma_{max})^{-2}$ employed in the methodology of Stanley and Chan [14] for the calculation of the stress intensity factor from thermoelastic data.

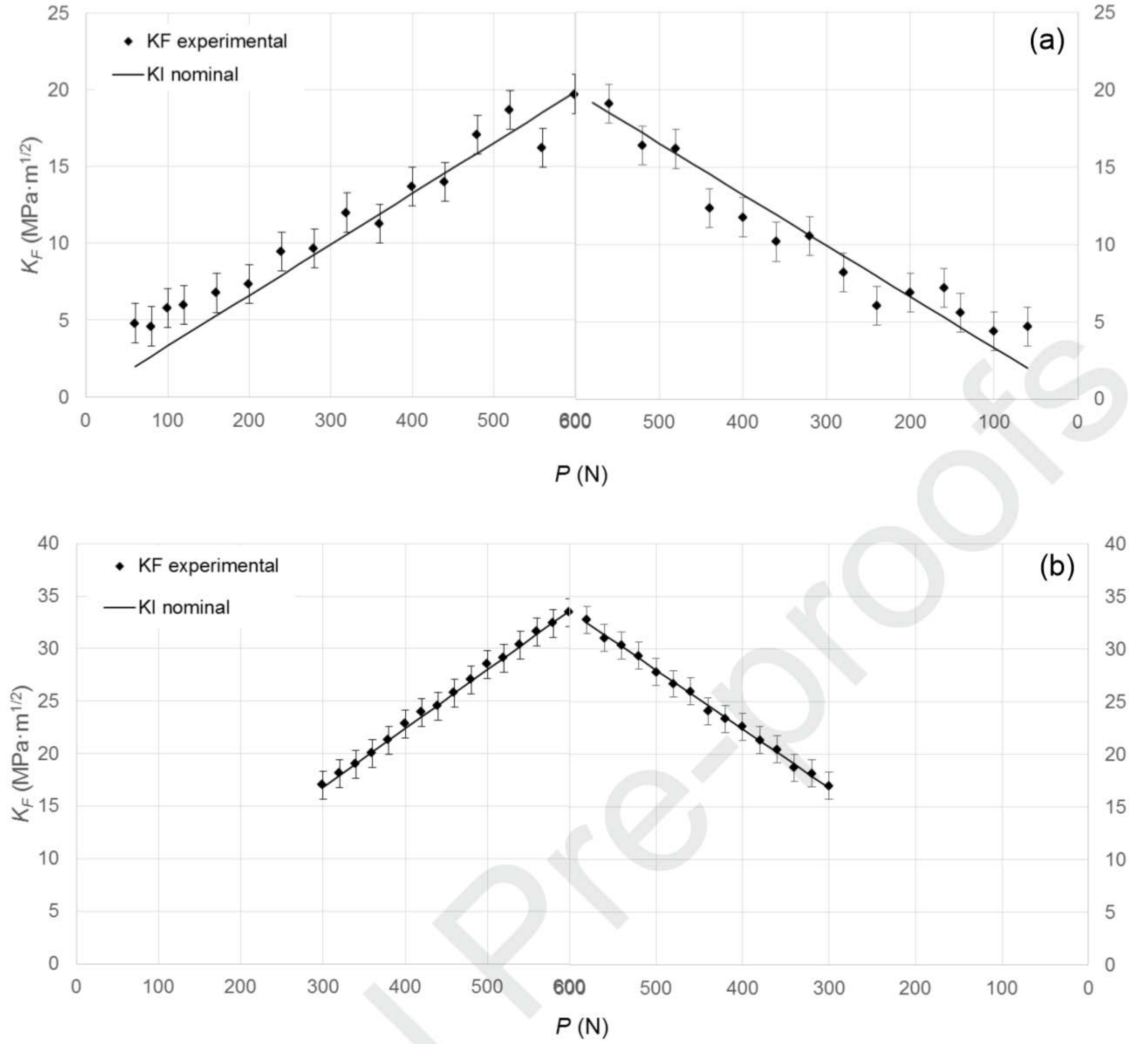

Figure 7 Variation of experimental K_F along a full loading cycle obtained using the CJP model [9] in combination with displacement data obtained using DIC technique for two different aluminium alloys at two different stress ratio values: (a) Al2024-T3 for a 4.63 mm crack at R=0.1 and (b) Al7050-T6 for a crack length of 8.63 mm at R=0.5.

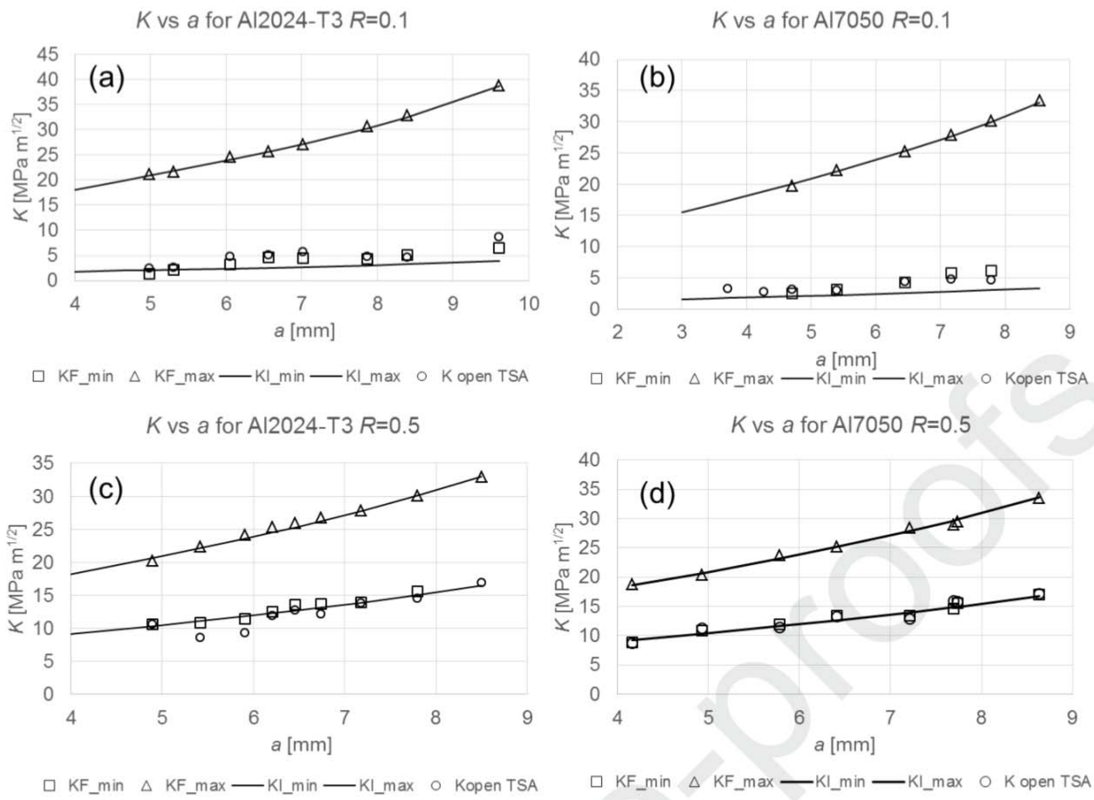

Figure 8 Comparison of experimental and nominal *K* values at different crack lengths for two aluminium alloys tested at two different stress ratio values: (a) Al2024-T3 at *R*=0.1, (b) Al7050 at *R*=0.1, (c) Al2024-T3 at *R*=0.5 and (d) Al7050-T6 at *R*=0.5.

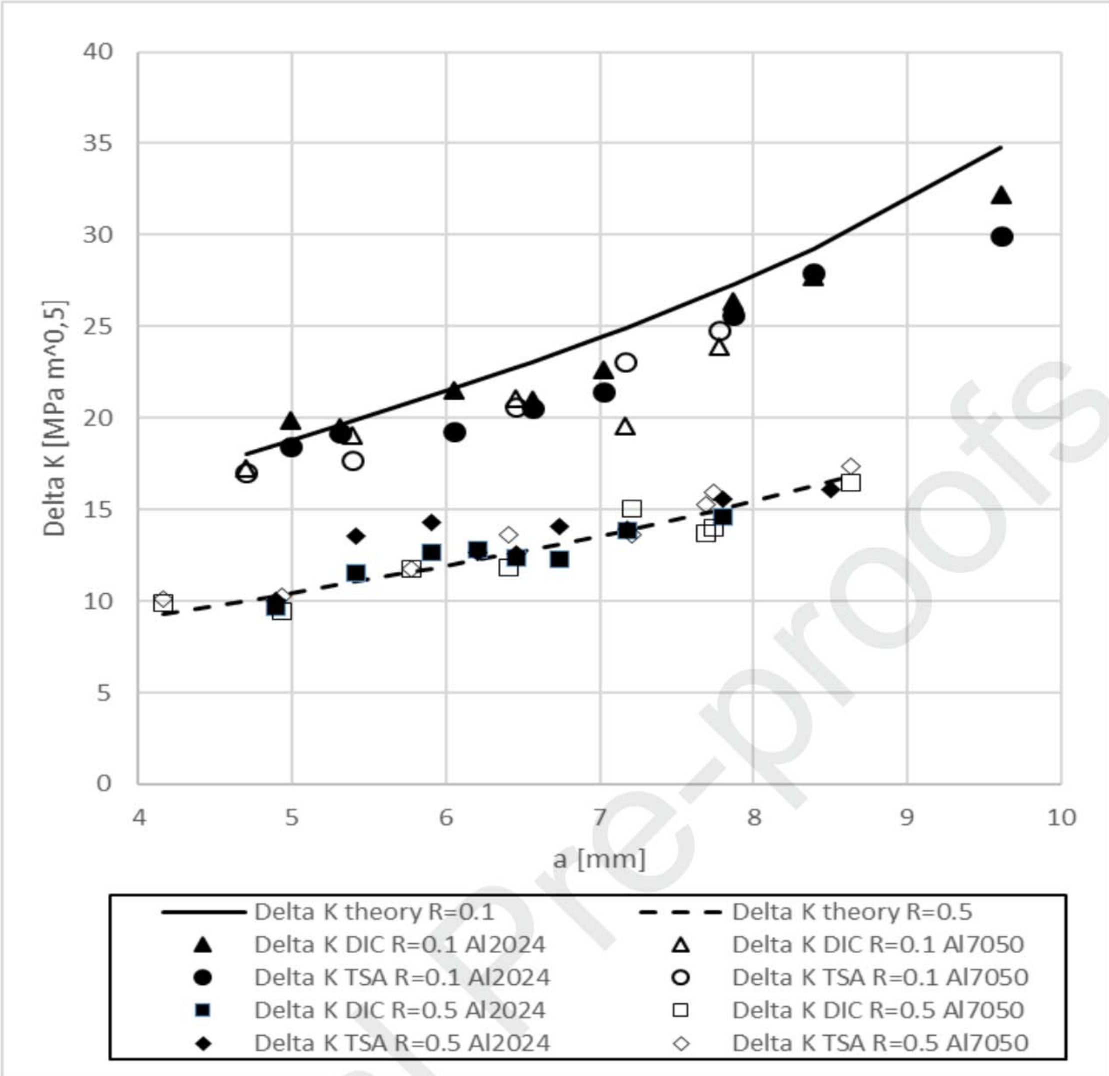

Figure 9 Comparison of ΔK nominal and ΔK effective obtained by DIC and TSA at different crack lengths. Experiments conducted for two aluminium alloys (Al2024-T3 and Al7050-T6) tested at two different R-ratios, namely R=0.1 and R=0.5.

Highlights:

- Calculation of effective stress intensity factor range by TSA and DIC.
- Combination of full-field optical techniques with models for characterising crack tip fields.
- Retardation effect on fatigue crack growth by analysing the range of stress intensity factor.
- Potential ability of TSA and DIC to account for the shielding effect during fatigue crack growth.

Declaration of interests

☒ The authors declare that they have no known competing financial interests or personal relationships that could have appeared to influence the work reported in this paper.

☐The authors declare the following financial interests/personal relationships which may be considered as potential competing interests: